Multiantenna-Based Data Filling Method for Retrieving Electron Density Profiles From GNSS Radio Occultation Data

Hyeyeon Chang, Woo Kyoung Lee, Hyosub Kil, Hyosang Yoon, and Jiyun Lee, *Member, IEEE*

***Abstract*— Retrieval of ionospheric electron density below low Earth orbit (LEO) altitude using global navigation satellite system radio occultation (RO) sounding requires total electron content (TEC) calibration by subtracting TEC on the non-occultation side from that on the occultation side. However, this calibration is not applicable to RO missions, where the occultation antennas cannot observe non-occultation side TEC. This article proposes a methodology for retrieving ionospheric electron density through multiantenna-based data filling. The non-occultation side TEC observed by using a precise orbit determination (POD) antenna data is connected to the occultation side TEC observed by an occultation antenna, enabling the application of the calibration technique. The methodology involves modeling TEC in the remaining gap between the data from POD and occultation antennas by utilizing the Epstein function with a varying scale height. The interior-point method is used to determine the optimal parameters for the function that best fits the observations. The proposed method is validated by applying it to Korean multipurpose satellite-5 (KOMPSAT-5) data and comparing the electron densities retrieved from KOMPSAT-5 data with collocated ionosonde observations. The results demonstrate that the electron density values retrieved by the proposed algorithm are in good agreement with those obtained from ionosonde measurements.**

***Index Terms*— Electron density retrieval, global navigation satellite system (GNSS) radio occultation (GNSS RO), ionosphere, total electron content (TEC) calibration.**

I. Introduction

THE ionosphere is part of Earth's upper atmosphere, situated at altitudes ranging from 75 to 1000 km above Earth's surface. Within this region, atoms and molecules are ionized, leading to an impact on the propagation of electromagnetic waves through the ionosphere. Therefore, monitoring the ionosphere is crucial for maintaining reliable radio communication and navigation systems, as well as for predicting and mitigating the effects of ionosphere-induced space weather on these systems. Traditional methods for observing and measuring the ionosphere rely on in situ measurements from satellites and rockets, and observations from ground-based instruments such as the network of global navigation satellite system (GNSS) reference stations, ionosondes, and incoherent scatter radars. Although these techniques provide accurate measurements, they suffer from limited global coverage. Ground-based measurements are restricted to specific locations, and in situ satellite and rocket measurements cover a small region at a time, resulting in incomplete and sparsely sampled data. The sparsity of data presents significant challenges in accurately characterizing the spatial and temporal variability of ionospheric processes and phenomena.

GNSS radio occultation (RO) has emerged as a complementary technique that can overcome the limitations of other sounding instruments [1]. GNSS RO is a remote sensing technique that observes Earth's atmosphere, including the ionosphere, based on the degree of refraction and delay in GNSS signals received from low Earth orbit (LEO) satellites. GNSS RO provides global coverage of Earth's ionosphere, including remote and oceanic regions where other ground-based monitoring techniques are not feasible, since the RO technique uses signals from GNSS constellations covering most of Earth's surface. In addition, the RO technique provides high vertical resolution measurements of electron density with a resolution of 1 km or better in the ionosphere. The global positioning system/meteorology (GPS/MET) experiment was a proof-of-concept mission for sounding Earth's atmosphere using the GNSS RO technique. This mission was highly successful in monitoring the ionosphere [2], [3], [4] and led to the development of several RO missions to provide ionospheric electron density profiles, including challenging minisatellite payload (CHAMP) [5], gravity recovery and climate experiment (GRACE), constellation observing system for meteorology, ionosphere and climate-1 (COSMIC-1) [6], [7], COSMIC-2 [8], [9], meteorological operational satellite-A (MetOp-A) [10], [11], Feng-Yun 3C [12], and Korean multipurpose satellite-5 (KOMPSAT-5) [13]. Due to the advantages of the GNSS RO technique, the demand for its data is increasing in various fields that require ionospheric observations and space weather monitoring. Electron density profiles from RO provide valuable resources for these purposes [14], [15], [16]. Furthermore, integrating RO-derived electron density profiles into the data assimilation process can improve the accuracy of atmospheric/ionospheric models, leading to

Manuscript received 30 December 2023; revised 3 June 2024 and 24 July 2024; accepted 18 August 2024. Date of publication 26 August 2024; date of current version 5 September 2024. This research was supported by the Korea Astronomy and Space Science Institute under the R&D program (Project No. 2024-1-9-0201) supervised by the Ministry of Science and ICT and the National Research Foundation of Korea funded by the Ministry of Science and ICT under Grant 2022M1A3C2069728, Future Space Education Center. The work of Hyosub Kil was supported by NSF under Grant AGS2029840. *(Corresponding author: Jiyun Lee.)*

Hyeyeon Chang, Hyosang Yoon, and Jiyun Lee are with the Department of Aerospace Engineering, Korea Advanced Institute of Science and Technology, Daejeon 305-701, South Korea (e-mail: cosmoshy93@gmail.com; hyosang.yoon@kaist.ac.kr; jiyunlee@kaist.ac.kr).

Woo Kyoung Lee is with Korea Astronomy and Space Science Institute, Daejeon 34055, South Korea (e-mail: wklee@kasi.re.kr).

Hyosub Kil is with the Johns Hopkins University Applied Physics Laboratory, Laurel, MD 20723 USA (e-mail: Hyosub.Kil@jhuapl.edu).

Digital Object Identifier 10.1109/TGRS.2024.3449337

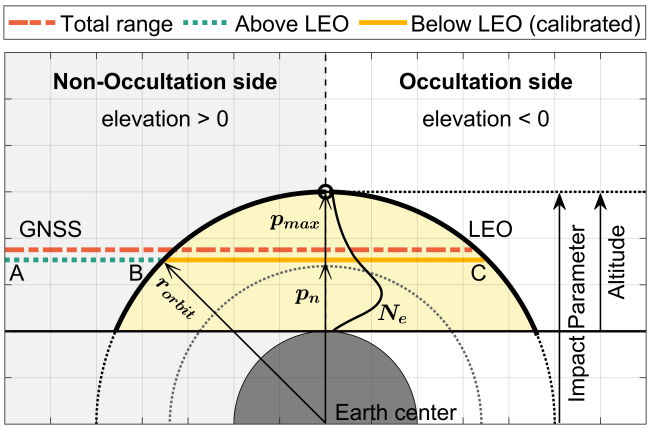

Fig. 1. 2-D geometry of an occultation event. The red dash-dotted line represents the ray path between the GNSS and LEO satellites during the occultation event. It contains both the section of the ray above the LEO altitude (green dotted line) and the section below the LEO altitude (yellow shadow with yellow solid line). The black circle denotes the point of the largest straight-line impact parameter.

a deeper understanding of both neutral states and space weather [17], [18].

Fig. 1 illustrates the GNSS RO technique using the 2-D geometry of an occultation event. In Fig. 1, r represents the distance between the Earth's geometric center and one point on the ray path, while p denotes the straight-line impact parameter. The straight-line impact parameter is defined as the perpendicular distance between Earth's center and the straight-line path followed by the ray approaching the atmosphere. The ray path between the GNSS and LEO satellites (red dash-dotted line) during the occultation event comprises both a section of the ray above the LEO altitude (green dotted line) and a section below it (yellow solid line within the yellow shadow). Therefore, correcting the contribution of ionospheric information above the LEO altitude is essential for accurately retrieving the electron density profile below the LEO altitude.

Initially, ionospheric information above the LEO altitude was replaced by a climate model or extrapolated based on information below the LEO altitude [2]. Schreiner et al. [3] introduced another technique that allows for a solution of ionospheric information below the LEO altitude only, without using ionospheric climatology or extrapolation for the ionosphere above the LEO altitude. This method involves utilizing observational data from both the ascending and descending parts of the LEO with respect to the point of the largest impact parameter. The observational data are the data that are continuously collected from a single pair consisting of a GNSS satellite and an antenna on the LEO satellite. The point of the largest straight-line impact parameter is marked with a black circle in Fig. 1. On the left side of the maximum straight-line impact parameter point is the "non-occultation side," where the elevation angle of the line-of-sight to the GNSS satellite at "A" is positive. On the right side is the "occultation side," where the elevation angle of the line-of-sight to the same GNSS satellite is negative. Assuming that the GNSS satellite is in the LEO plane, and the LEO is close to circular, the data on the non-occultation side (data along the section "AB") are subtracted from the occultation side data (data along the section "AC") at the given straight-line impact parameter. This process yields ionospheric information below the LEO altitude, and the resulting data are referred to as "calibrated" ionospheric information (information along the section "BC"). In [3], it was stated that this calibration technique introduces errors (e.g., due to horizontal inhomogeneity of electron density) that are statistically closer to zero than those introduced by using climatology or extrapolating observational data. The term "calibration technique" in this article refers to the method described in [3].

However, this calibration technique is applicable only when the non-occultation side observations are available. The availability of observations on the non-occultation side depends on the viewing geometry and data coverage of antennas used to probe the ionosphere below the LEO altitude. There are two types of antennas in RO missions: precise orbit determination (POD) and occultation antennas. The POD antennas are used to determine the precise orbit of the LEO satellite (as the name implies), while the occultation antennas are used to retrieve atmospheric/ionospheric profiles. Fig. 2 depicts a simple illustration of the antenna placements and data coverage of several missions. While the POD antennas of CHAMP, GRACE, MetOp-A, and KOMPSAT-5 are mounted in the zenith direction, the POD antennas of COSMIC-1 and COSMIC-2 are tilted approximately 75° from the zenith to allow ionospheric profiling via the occultation technique [19], [20], [21]. The POD antennas of COSMIC satellites can continuously track the same GNSS satellite on both the occultation side (i.e., negative elevation) and the non-occultation side (i.e., positive elevation). Therefore, the calibration technique can be applied. The CHAMP, GRACE, MetOp-A, and KOMPSAT-5 utilize limb pointing (fore-/aft-looking) occultation antennas to monitor the ionosphere below the LEO altitude. Unlike the POD antennas on COSMIC missions, the occultation antennas on these missions lack the capability to observe the non-occultation side. This is because the same GNSS satellite tracked as an occulting satellite would be above the local horizon of LEO on the non-occultation side, while the maximum observational altitudes are limited to near or below the LEO altitudes.

Other methods can be applied in the absence of observations on the non-occultation side. In studies [5], [10], and [22], a model-assisted technique was applied where the ionosphere and plasmasphere above the LEO altitude were modeled by a Chapman layer function superposed with an exponential decay function. Model parameters were determined by an iterative process to obtain a smooth transition between model outcomes and measurements obtained from the occultation antenna. The results in [10] validated that the model-assisted technique can successfully retrieve the electron density profiles from the MetOp-A data. However, the estimation accuracy can vary depending on the models used and the quantity of available observations. In studies [23] and [24], the ionospheric information above the LEO altitude was computed from POD antenna measurements using a dual-layer tomographic voxel model outlined in [25]. The electron content above the LEO altitude was implemented and solved in a Kalman filter, utilizing all the GNSS observations above the LEO altitude. The method includes smoothing with a low-degree

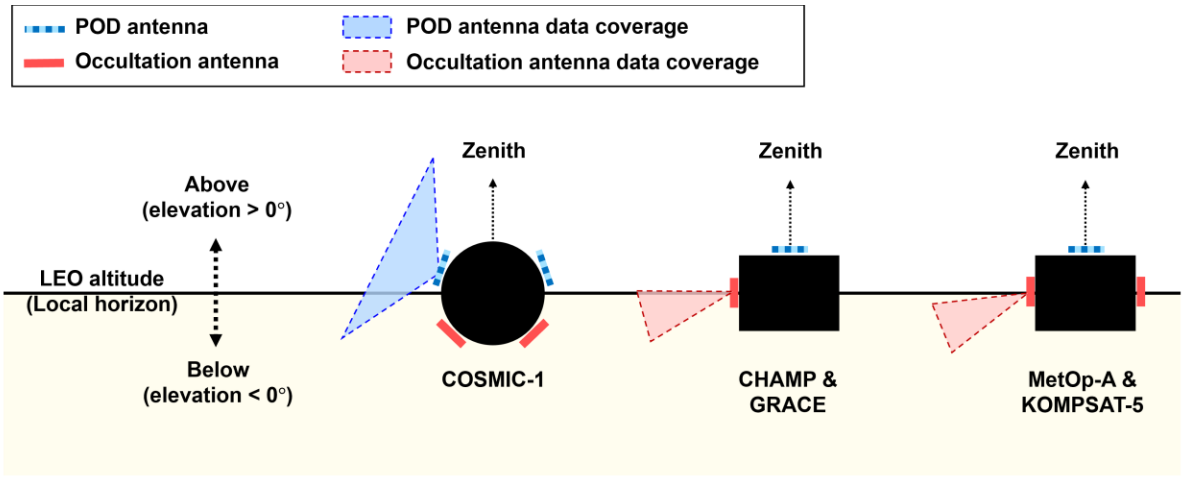

Fig. 2. Schematic illustration of the POD and occultation antenna placements on COSMIC-1, CHAMP, GRACE, MetOp-A, and KOMPSAT-5 satellites. The shaded areas with dashed outlines depict the vertical coverages of data from the antennas used for ionospheric occultation.

polynomial to remove any discontinuities associated with the grid tomographic estimation. The results in [23] showed an improvement in the retrieved electron density profile by applying the dual-layer tomographic plasmaspheric correction. However, the accuracy of tomographic estimation strongly relies on the spatial/temporal resolution of the grid and the coverage of observations. In addition, there could be additional errors owing to the smoothing process.

In this study, we identify that a POD antenna on the non-occultation side can track the same GNSS satellite as tracked by an occultation antenna on the occultation side. Therefore, by simply connecting the data from the POD and occultation antennas, we can apply the calibration technique, avoiding solely relying on models. This technique also alleviates the need for a tomographic model for the above LEO altitude. Based on these capabilities, we propose the multiantenna-based data filling method, which utilizes observations from both POD and occultation antennas to retrieve electron density profiles. After filling the non-occultation side using observations from the POD antenna, a data gap may remain between the observations from the POD and occultation antennas. Our proposed method involves modeling the remaining data gap between the observations obtained from the two different antennas and connecting them. For validation of our method, we apply the proposed method to the KOMPSAT-5 data and retrieve the electron density profiles from it. To validate the algorithm for modeling the remaining data gap, a data gap was artificially introduced into a profile that originally had no gap, and the output of the algorithm was compared with the original profile. Additionally, the proposed method underwent validation through a comparison of the electron density profiles retrieved from KOMPSAT-5 data with ionosonde observations.

The rest of this article is organized as follows. Section II provides an overview of the electron density retrieval method used in this study. Section III describes the coverage and data connectivity of the POD and occultation antennas. Section IV outlines our proposed multiantenna-based data gap filling method. In Section V, we apply the proposed method to KOMPSAT-5 and validate it by comparing the electron density profiles retrieved from the arbitrarily truncated data and the original data. Additionally, we compare the electron density retrieved from the KOMPSAT-5 data with that from the ionosonde instruments. Finally, Section VI presents our concluding remarks.

II. Overview of Ionospheric Electron Density Retrieval

This section describes the process of electron density retrieval with the calibration technique used for obtaining ionospheric information below the LEO altitude.

In this study, the electron density is retrieved using Abel inversion through total electron content (TEC) data. Dual-frequency carrier phase measurements are used to estimate the TEC between the GNSS and LEO satellites. The Abel inversion through TEC assumes spherical symmetry and straight-line propagation. Assuming spherical symmetry means that the electron density varies only in the vertical direction and is horizontally homogeneous. Strong horizontal gradients can lead to significant errors in the retrieved electron density profiles [3], [26], [27]. Nonetheless, the Abel inversion with the spherical symmetry assumption is the robust and simple method for obtaining the electron density profile. The assumption of straight-line propagation implies that signals in two frequencies travel along the same ray path. It was demonstrated that, for GNSS frequencies, ray separation from straight-line propagation for observations in LEO is small (about several kilometers or less) as compared with the vertical scale of the ionospheric $F2$ layer [3]. Therefore, the assumption of straight-line propagation introduces minor errors when monitoring the $F2$ layer.

The expression of GNSS carrier phase (L_1, L_2) observables for two signal frequencies (f_1, f_2) is presented in their general form as follows (in distance units) [28], [29]:

$$L_1 = \text{range} - \frac{I}{f_1^2} + \lambda_1 N_1 + B_1 + \varepsilon_1$$
$$L_2 = \text{range} - \frac{I}{f_2^2} + \lambda_2 N_2 + B_2 + \varepsilon_2. \quad (1)$$

range refers to the summation of the true range between GNSS and LEO satellites, along with satellite/receiver clock biases, tropospheric error, and non-dispersive delays in hardware signal paths. The carrier phase observables contain an integer ambiguity, $\lambda_i N_i$ $(i = 1, 2)$, where λ_i is the carrier wavelength at frequency f_i. The term ε indicates the low levels of multipath and thermal noise errors compared to the code measurements. I/f_i^2 denotes the ionospheric delay at frequency f_i. B_i is the dispersive components of the satellite and receiver instrumental phase delay biases at frequency f_i. In this study, we do not include a centimeter-level phase wind-up term in (1), assuming it has been corrected as discussed in [30].

Using the assumption of straight-line propagation, the TEC can be expressed as the following equation:

$$\mathrm{TEC} = \frac{f_1^2 f_2^2 (L_1 - L_2)}{40.3\left(f_1^2 - f_2^2\right)} = \mathrm{TEC}_{\mathrm{true}} + \mathrm{Bias}_N + \mathrm{Bias}_B$$

where

$$\mathrm{Bias}_N = \frac{f_1^2 f_2^2}{40.3\left(f_1^2 - f_2^2\right)}\left(\lambda_1 N_1 - \lambda_2 N_2\right)$$
$$\mathrm{Bias}_B = \frac{f_1^2 f_2^2}{40.3\left(f_1^2 - f_2^2\right)}(B_1 - B_2). \tag{2}$$

The TEC in (2) includes not only the true TEC ($\mathrm{TEC}_{\mathrm{true}}$), but also the bias error caused by integer ambiguities (Bias_N) and inter-frequency biases (Bias_B).

To obtain the ionospheric information below the LEO altitude, it is necessary to remove the ionospheric contribution above the LEO altitude. In [3], this is done through the calibration process. The calibrated TEC can be estimated by using the following equation:

$$\mathrm{TEC}_{\mathrm{calibrated}} = \mathrm{TEC}_{\mathrm{Occultation\ side}} - \mathrm{TEC}_{\mathrm{Non\text{-}Occultation\ side}}. \tag{3}$$

$\mathrm{TEC}_{\mathrm{Occultation\ side}}$ is the observational TEC along the ray connecting the GNSS and LEO satellites on the occultation side. $\mathrm{TEC}_{\mathrm{Non\text{-}Occultation\ side}}$ is the observational TEC on the non-occultation side, corresponding to the ascending/descending part for the setting/rising occultation event. During the calibration process, the bias terms in (2) are canceled out if the observations are obtained from the same receiver and transmitter within an arc of continuous observations, as there would be no change in bias terms [31]. After obtaining the calibrated TEC, it can be related to electron density ($N_e(r)$) through (4), under the assumption of spherical symmetry [3]

$$\mathrm{TEC}_{\mathrm{calibrated}}(p) = 2\int_p^{p_{\mathrm{orbit}}} \frac{r N_e(r)}{\sqrt{r^2 - p^2}} dr \tag{4}$$

where r is the radius and p is the straight-line impact parameter. Under the assumption of spherical symmetry, the electron density can be expressed as a function of radius, such that $N_e = N_e(r)$. The electron density can be derived by using the Abel inversion as in (5) [3]

$$N_e(r) = -\frac{1}{\pi}\int_r^{p_{\mathrm{orbit}}} \frac{d\mathrm{TEC}_{\mathrm{calibrated}}/dp}{\sqrt{p^2 - r^2}} dp. \tag{5}$$

Equation (5) can be analytically solved by (6) as a function of the straight-line impact parameter [32]

$$N_e(p_i) = \frac{3}{4}\frac{\mathrm{TEC}(p_i)}{\sqrt{2p_i(p_{i+1} - p_i)}} - \sum_{k=1}^{n-i} c_{k,i} N_e(p_{i+k}). \tag{6}$$

p_i is the straight-line impact parameter that has the same magnitude as the radius (r) at the ith spherical layer. The coefficients ($c_{k,i}$) are derived in [33].

Assuming constant electron density in the upper most layers around the orbit altitude, the TEC near the orbit altitude can be written approximately as (7), which is derived from (4) [34]

$$\mathrm{TEC}_{\mathrm{calibrated}}(p) \approx 2N_e(p_{\max})\sqrt{2p_{\max}(p_{\max} - p)} \tag{7}$$

where $p_{\max}$ is the maximum straight-line impact parameter, assumed to be equal to the orbit radius ("orbit altitude" above the Earth's surface). The electron density at the orbit altitude ($N_e(p_{\max})$) is found by linear regression of the square of the calibrated TEC for the uppermost few kilometers (about 10 km) of the straight-line impact parameters. Starting from the highest altitude, the final electron density profile is obtained sequentially down to the lower altitudes, which is why this method is also called the "onion peeling" method [35].

III. Coverage and Data Connectivity of POD and Occultation Antennas

In this section, we examine the coverage and data connectivity of the POD and occultation antennas. The top row of Fig. 3 displays the percentage distributions of elevation angles from the POD (POD) and occultation (OCC) antenna data gathered on a single day for: 1) COSMIC-1 (March 7, 2013); 2) CHAMP (January 5, 2008); and 3) KOMPSAT-5 (January 7, 2020). The days are randomly selected because the results for any day are similar. Five LEO satellites of the COSMIC-1 mission were available, while CHAMP and KOMPSAT-5 each had one LEO satellite. Each bar represents the percentage of the data points within a 2° elevation angle bin relative to the total data points across all elevation angles. The percentages for the POD and occultation antennas are calculated separately. The COSMIC-1 satellite is equipped with the POD antenna whose boresight vector is tilted toward the flight direction, enabling it to observe both the non-occultation (Non) and occultation (Occ) sides. The distribution of data points for negative elevation angles is attributed to the tilt of the POD antenna. For CHAMP, the POD and occultation antennas provide observations on the non-occultation (i.e., positive elevation) and occultation (i.e., negative elevation) sides, respectively. The KOMPSAT-5's data point distribution is comparable to that of CHAMP, but its POD antenna can cover parts of the occultation side (negative elevation), indicating its ability to track signals below the local horizon of the LEO satellite. This capability can be attributed to the boresight of the POD antenna. Since KOMPSAT-5 was primarily designed to provide synthetic aperture radar images, the spacecraft was tilted from the zenith regularly [36], potentially leading to a more extensive negative elevation coverage compared to CHAMP. The difference in the OCC

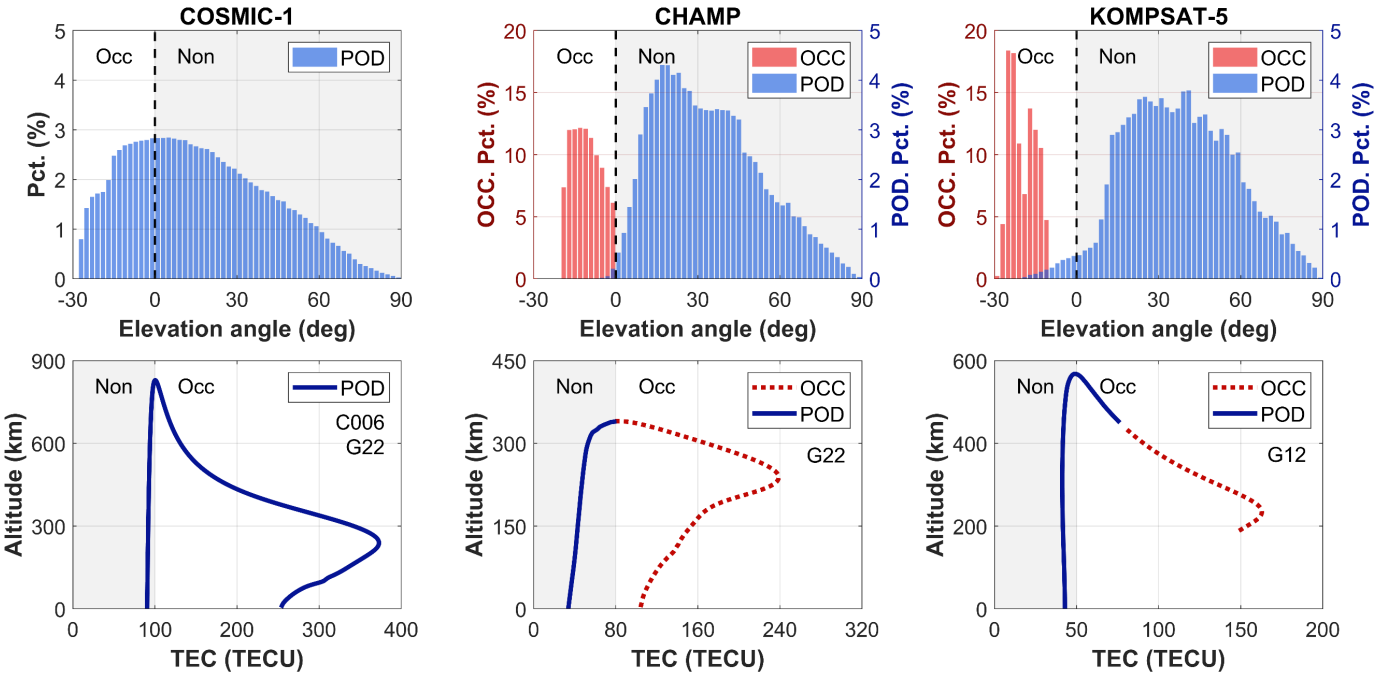

(a) (b) (c)

Fig. 3. Coverages of the POD and occultation antennas on the non-occultation (gray) and occultation (white) sides on a single day for (a) COSMIC-1 (March 7, 2013), (b) CHAMP (January 5, 2008), and (c) KOMPSAT-5 (January 7, 2020). The top row shows the distributions of elevation angles from the POD (blue bars) and occultation (OCC) antenna data (red bars). The bottom row illustrates examples of TEC from the POD (blue solid curves) and the occultation antennas (red dotted curves) tracking the same GNSS satellites during their ascending and descending parts of the LEO satellite with respect to the point of maximal straight-line impact parameter.

distributions between Fig. 3(b) and (c) can be attributed to the difference in the occultation antenna boresights on the CHAMP and KOMPSAT-5 satellites.

The bottom row in Fig. 3 presents TEC profiles as a function of altitude, acquired through tracking a GNSS satellite. TEC retrievals from POD and occultation antennas are shown by blue solid and red dotted curves, respectively. The bottom part of Fig. 3(a) shows an event where the POD antenna of a COSMIC-1 satellite C006 tracks the GPS PRN 22 satellite. As the TEC data from this event covers both non-occultation and occultation sides within a continuous arc, the calibrated TEC can be estimated by directly subtracting the non-occultation side TEC from the occultation side TEC. On the other hand, missions such as CHAMP and KOMPSAT-5 use occultation antennas to monitor the ionosphere below the LEO altitude. These antennas track signals only in negative elevation angles with respect to the LEO local horizon and provide data only on the occultation side [red dotted curves in Fig. 3(b) and (c)]. Therefore, the calibration technique, which requires the availability of data from the same GNSS satellite being tracked during both ascending and descending phases, is not applicable.

However, the POD antennas on the CHAMP and KOMPSAT-5 satellites can track the GNSS satellite above the LEO altitude on the non-occultation side. This implies that during an event where the ascending and descending LEO satellite tracks the same GNSS satellite, the POD antenna covers the non-occultation side while the occultation antenna covers the occultation side. Consequently, the data from these antennas can be connected to apply the calibration technique. The CHAMP example in the bottom panel of Fig. 3(b) reveals that the POD antenna can track GPS PRN 22 on the non-occultation side up to the top altitude, while the occultation antenna tracks the same GNSS satellite from the top to the lower altitudes on the occultation side. By connecting them, we can differentiate them for a given altitude, to calculate the calibrated TEC. For KOMPSAT-5, although the occultation antenna cannot track GPS PRN 12 up to the top altitude, the POD antenna can cover some parts of the occultation side, indicating its ability to track signals below the LEO local horizon. This capability is attributed to the boresight of the POD antenna, as previously mentioned.

While the cases depicted in the bottom panels of Fig. 3(b) and (c) show either no gap or a small gap between the data from the POD and occultation antennas, it is important to note that in many cases, this gap can be significantly larger. This study specifically focuses on scenarios where there is no gap between the data from the two antennas and where the POD antenna can cover some portions of the occultation side despite a gap. The primary aim of this study is to verify the use of the POD antenna data for filling in non-occultation side observations and enabling the calibration technique. As part of future work, we plan to extend our algorithm to handle larger gaps, such as cases where there is no available data near or at the top altitude from either the POD or occultation antenna.

IV. Multiantenna-Based Data Filling Method

This section presents a multiantenna-based data gap filling method. Instead of modeling the entire ionosphere above

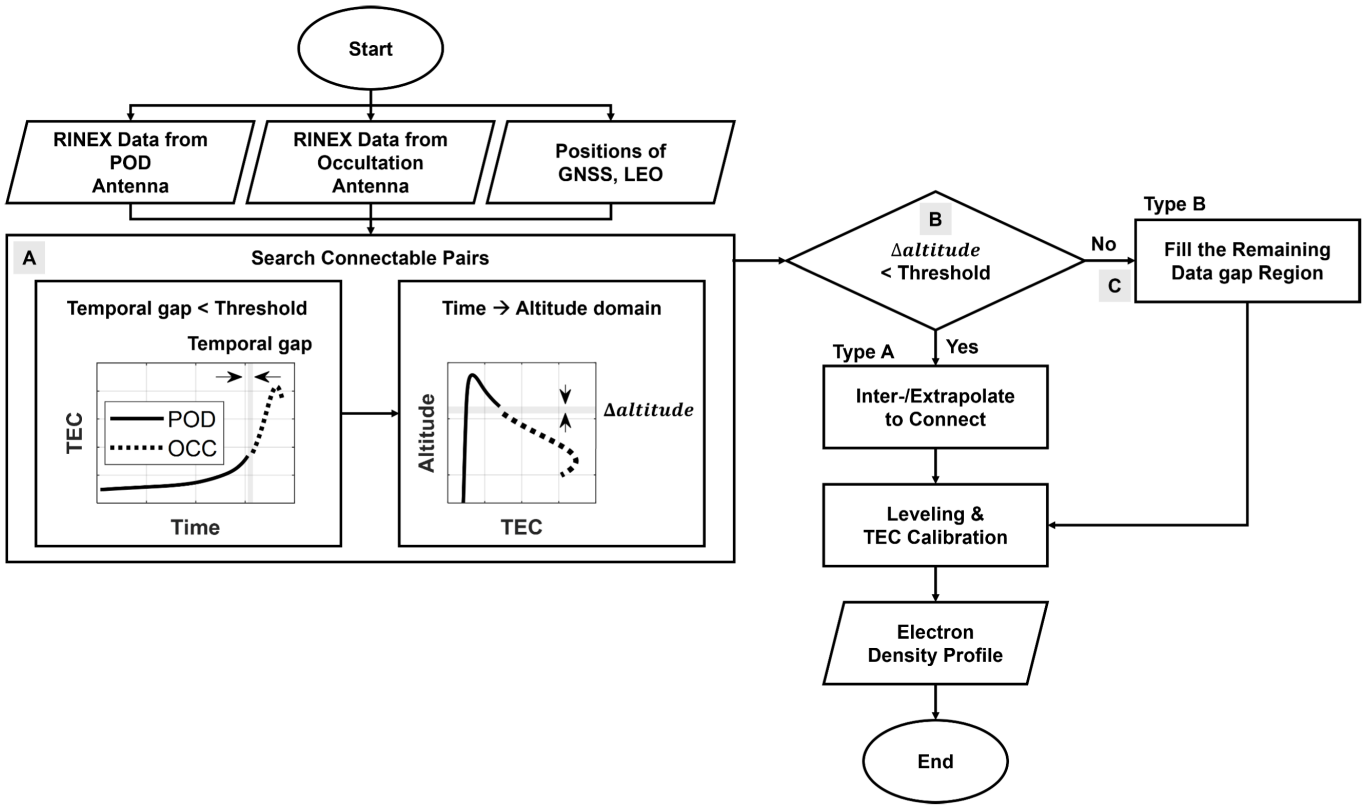

Fig. 4. Flowchart of the proposed multiantenna-based data gap filling method. "A," "B," and "C" correspond to the sections in Section IV.

the LEO altitude or employing a tomographic model, this approach directly uses ionospheric observations from the POD antenna, which tracks the same GNSS satellite tracked by the occultation antenna on the occultation side. By filling the TEC above the LEO altitude with the observations from the POD antenna and connecting it to the TEC from the occultation antenna, the TEC can be calibrated by applying the same process utilized for the COSMIC missions.

Fig. 4 shows an overview of the proposed multiantenna-based data gap filling method. The input data consist of receiver independent exchange format (RINEX) data from both the POD and occultation antennas, as well as the positions of the GNSS and LEO satellites. The details of each procedure are explained as follows.

A. Search for the Pairs That Can Be Connected

In this study, we only connect pairs where both the POD and occultation antenna data are present within a continuous ascending and descending event. The first task is to identify the data pair from the POD and occultation antennas that was transmitted from the same GNSS satellite. At this step, we estimate TEC in the time domain using the methodology described in Section II. For pre-processing, outliers due to cycle slips are detected and removed. Then, the TEC observations from the POD and occultation antennas for each GNSS satellite are combined. For a single GNSS satellite, the time interval between consecutive occultation events is more than an hour. A temporal threshold of 30 min is applied to differentiate between separate occultation events. If the temporal gap between the POD antenna and occultation antenna data is smaller than the threshold, we identify that the POD antenna data contain information on the non-occultation side, allowing them to be connected for the calibration technique. Next, TEC is converted from the time domain to the altitude domain (i.e., straight-line impact parameter domain).

B. Categorization Into Two Types (Type A and Type B) According to Altitude Gap

As mentioned previously, our investigation focuses on two cases: 1) where there is no data gap between the two antennas' data and 2) where a gap exists, but the POD antenna data can cover some parts of the occultation side. The connectable pairs can be categorized into two types according to an altitude gap. Fig. 5 shows examples of two types from KOMPSAT-5 data: 1) Type A where there is no gap and 2) Type B where there is a gap, with the POD antenna data covering some portions of the occultation side. The black solid curve represents TEC observed from the POD antenna and the black dotted curve is TEC observed from the occultation antenna. The altitude gap (Δaltitude) is the vertical distance between the altitude of the POD antenna TEC termination at the occultation side and the altitude of the occultation antenna TEC termination. If the altitude gap of a specific event is smaller than a defined threshold, the event is defined as "no gap" (i.e., Type A). In this study, the threshold is set to be 5% of the orbit altitude. For example, if we take the KOMPSAT-5 data with an orbit altitude of approximately 560 km, the threshold would be around 28 km. With a threshold of 28 km, a Δaltitude smaller

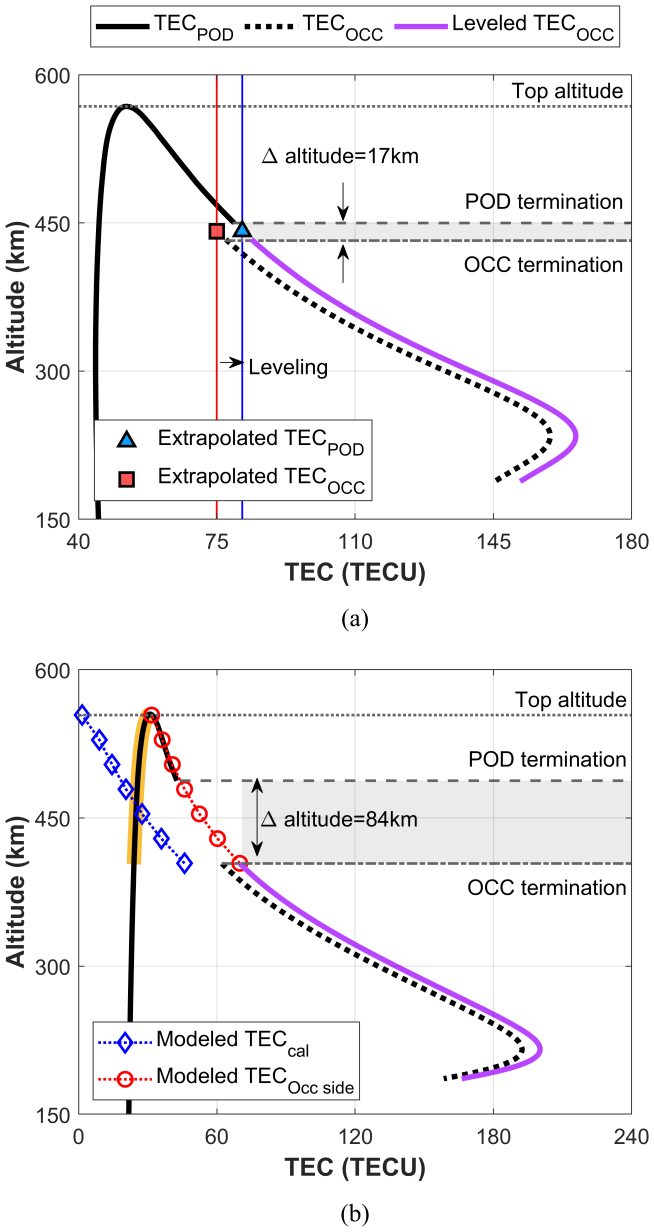

Fig. 5. Illustration of the two types from KOMPSAT-5. (a) Type A and (b) Type B. (a) For Type A, extrapolation (or interpolation) is used to connect the POD antenna data (black solid curve) and occultation antenna data (black dotted curve). After obtaining the extrapolated values (blue triangle and red square), the difference between those values is added to the occultation antenna data, resulting in the leveled occultation antenna TEC (purple solid curve). (b) For Type B, the method for filling the remaining data gap (gray shadow region) is applied to connect the data from the two antennas. First, we model the calibrated TEC (blue dotted curve with diamonds) and add the non-occultation side TEC (black solid curve highlighted in yellow) to obtain the modeled occultation side TEC (red dotted curve with circles). Subsequently, the TEC from the occultation antenna is leveled to align with the modeled occultation side TEC.

than 28 km is categorized as Type A [Fig. 5(a)], and larger than 28 km is categorized as Type B [Fig. 5(b)].

For Type A, we apply cubic spline extrapolation to connect the POD and occultation antenna data. If there is data overlap, interpolation method is used for their connection. Fig. 5(a) shows an example of Type A obtained from KOMPSAT-5 data, which has an altitude gap of approximately 17 km. We define the middle altitude between the altitude gap as the connecting altitude. The blue triangle point in Fig. 5(a) shows the extrapolation from the POD antenna data at the connecting altitude, and the red square point is the extrapolation result from the occultation antenna data at the connecting altitude. A bias is evident between the two extrapolation results, which can be attributed to a difference in bias values [in (2)] for each observation. Equations (8) and (9) describe the non-occultation side TEC from the POD antenna and the occultation side TEC from the occultation antenna, respectively. The Bias($=\text{Bias}_N + \text{Bias}_B$) for each antenna would be different because of antenna hardware differences. Without correcting this bias difference during calibration, an uncorrected bias will remain. Therefore, the leveling process is essential to obtain accurate TEC estimates by mitigating the effect of bias difference. Leveling is conducted by adding the amount of bias difference to the TEC from the occultation antenna. The leveled occultation side TEC (Leveled Occ. side TEC_{OCC}) from the occultation antenna has the same Bias as the POD antenna data, as indicated in (10). Thus, the remaining bias (Bias_{POD}) can be removed during the TEC calibration process by subtracting (8) from (10). The TEC from the occultation antenna, after leveling, is represented as the solid purple curve in Fig. 5(a)

$$\text{Non. Occ. side TEC}_{\text{POD}} = \text{Non. Occ. side TEC}_{\text{true}} + \text{Bias}_{\text{POD}} \tag{8}$$

$$\text{Occ. side TEC}_{\text{OCC}} = \text{Occ. side TEC}_{\text{true}} + \text{Bias}_{\text{OCC}} \tag{9}$$

$$\begin{aligned}\text{Leveled Occ. side TEC}_{\text{OCC}} &= \text{Occ. side TEC}_{\text{true}} + \text{Bias}_{\text{OCC}} + (\text{Bias}_{\text{POD}} - \text{Bias}_{\text{OCC}}) \\ &= \text{Occ. side TEC}_{\text{true}} + \text{Bias}_{\text{POD}}.\end{aligned} \tag{10}$$

However, for Type B [Fig. 5(b)], connecting the data from the POD and occultation antennas by extrapolation is challenging due to the presence of a large remaining data gap (i.e., large Δaltitude). Therefore, to connect the observations from two different antennas for Type B, it is necessary to fill the remaining gap by modeling.

C. Filling the Remaining Data Gap Region

This section proposes an algorithm for filling the remaining data gap between the data from the POD and occultation antennas to connect the data from both antennas.

We use an electron density model to fill the remaining data gap that exists above the density peak altitude (i.e., topside). Several analytical functions are available for electron density reconstruction, including exponential, alpha/beta Chapman, and Epstein [37], [38], [39], [40], [41]. We have chosen the Epstein function with a varying scale height (H) for two main reasons: 1) a varying H is necessary to model the electron density profile more realistically by reflecting its actual behavior and 2) H can be modeled linearly using the Epstein layer equation in a straightforward manner.

The Epstein (sech-squared) layer is defined as

$$N_e(p) = 4N_e(p_{hmF2}) \times \frac{\exp\left(\frac{p-p_{hmF2}}{H}\right)}{\left[1+\exp\left(\frac{p-p_{hmF2}}{H}\right)\right]^2} \tag{11}$$

where $N_e(p_{hmF2})$ and p_{hmF2} are the $F2$ peak density and its height, respectively. According to the above equation, H for the Epstein function can be directly calculated by the following equation [42], [43]:

$$H(p) = \frac{p - p_{hmF2}}{\ln\left[\frac{1}{N_e(p)}(2N_e(p_{hmF2}) - N_e(p) + A)\right]} \tag{12}$$

where

$$A = 2\sqrt{N_e(p_{hmF2})^2 - N_e(p)N_e(p_{hmF2})}.$$

Fig. 6 shows the comparison between results from applying a constant H and a varying H. The black solid curve in Fig. 6(a) represents the electron density profile retrieved from a KOMPSAT-5 Type A event. The curves with red triangles and purple squares depict the electron density reconstructed from the Epstein layer by applying constant H values. The curve with yellow circle markers represents the density profile obtained by applying (12) in the Epstein layer equation. According to Fig. 6(a), the electron density profiles modeled with constant H values (red curve with triangles and purple curve with squares) are hard to match with the true profile. In contrast, when the varying H is applied (yellow circles), the modeled profile shows good agreement with the true electron density profile. This is evident because the varying H is directly measured from the true electron density profile by (12). Fig. 6(b) shows the values of H as a function of altitude. The varying H can be fit into a linear function as shown by the dotted line with light-blue color, aligning with the previous findings outlined in [42] and [43].

By utilizing the linear trend of the effective scale height, (12) is simplified to the following linear form, as derived in [42]:

$$H(p) = \frac{dH}{dp}(p - p_{hmF2}) + H_0. \tag{13}$$

To model the remaining data gap region by applying the Epstein layer with a varying H, which is the combination of (11) and (13), we have to find the optimum pair of three parameters: $N_e(p_{hmF2})$, H_0, and dH/dp. Fig. 7 shows the flowchart for searching the optimum pair of parameters. To conduct the optimum pair search, we use the interior-point method which is one of the most promising methods for the numerical solution of constrained nonlinear optimization problems [44], [45]. At each iteration, the interior-point method computes the gradient and Hessian of the objective function, which represent the direction and rate of change of the function, respectively. Based on these calculations, the interior-point method determines the direction to move in the space of possible solutions to the problem and how far to move in that direction.

The first step for finding the optimum pair is to set the initial range (lower bound and upper bound) of the three parameters. The initial values are the midpoint of each range. In this study,

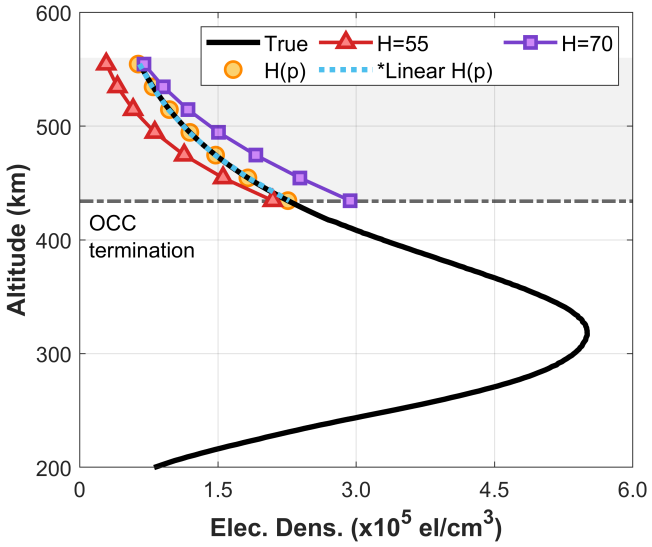

(a)

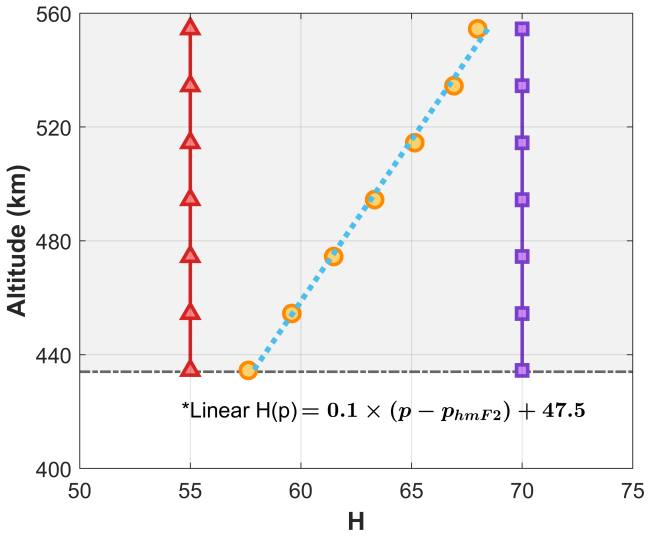

(b)

Fig. 6. Comparison of electron density profiles for different scale heights (H) for a KOMPSAT-5 Type A event. (a) Extension of the observed electron density profile (black solid curve) to above the occultation antenna TEC termination altitude using the Epstein function with different scale heights. The reconstructed electron density profiles using the Epstein function with constant H values (55, 70) are shown with red triangle and purple square symbols. The profile reconstructed using the Epstein function with a varying H is shown with yellow circles, while the profile from a linearly fit H is illustrated by a light-blue dotted line. (b) H profiles used for (a).

we set the initial range to 0 to 20 $\times$ 10^5 el/cm^3 for $N_e(p_{hmF2})$, 0–80 km for H_0, and 0 to 0.3 for dH/dp.

Afterward, we model the TEC on the occultation side from the altitude at which the data from the occultation antenna terminates (p_1) up to the orbit altitude (p_n) as a function of the straight-line impact parameter, using the initial parameter values.

To model the occultation side TEC, we first model the TEC along the section of the ray below the LEO altitude (i.e., calibrated TEC) from the altitude of occultation antenna TEC termination to the top altitude (i.e., orbit altitude). The

$$\text{modeled TEC}_{\text{calibrated}} = 2 \times \begin{pmatrix} \sqrt{r_1^2 - p_1^2} & \sqrt{r_2^2 - p_1^2} - \sqrt{r_1^2 - p_1^2} & \cdots & \sqrt{r_n^2 - p_1^2} - \sqrt{r_{n-1}^2 - p_1^2} \\ 0 & \sqrt{r_2^2 - p_2^2} & \cdots & \sqrt{r_n^2 - p_2^2} - \sqrt{r_{n-1}^2 - p_2^2} \\ \vdots & \vdots & \ddots & \vdots \\ 0 & 0 & \cdots & \sqrt{r_n^2 - p_n^2} \end{pmatrix} \times \begin{pmatrix} N_e(p_1) \\ N_e(p_2) \\ \vdots \\ N_e(p_n) \end{pmatrix} \tag{14}$$

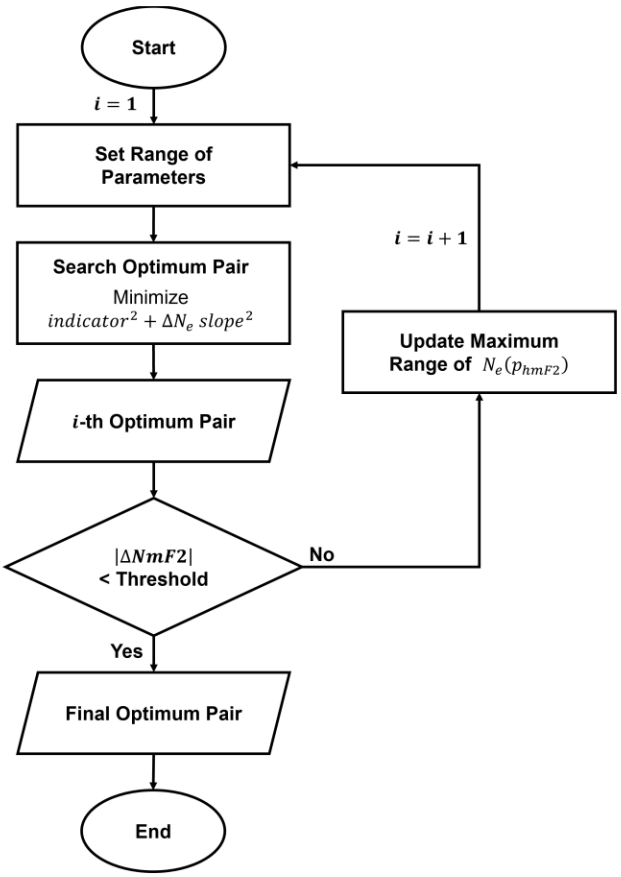

Fig. 7. Flowchart for searching the optimum pair of model parameters.

TEC below the LEO altitude can be estimated by using (14), as shown at the top of the page, under the assumption of spherical symmetry, where r is the radius, p is the straight-line impact parameter, and $N_e(p)$ is the electron density derived by applying the initial parameter values to the combination of (11) and (13). The ith row of the first matrix in (14), including "2×," represents the length of the ith ray path below the LEO altitude. The modeled calibrated TEC profile is depicted by the blue dotted curve with diamond markers in Fig. 5(b). We then add the non-occultation side TEC at the corresponding altitude to obtain the occultation side TEC. The non-occultation side TEC used for this calculation is highlighted in yellow in Fig. 5(b). The modeled TEC on the occultation side is shown by the red dotted curve with circle markers in Fig. 5(b).

Afterward, following the same process as Type A, we level the TEC observed by the occultation antenna to the modeled occultation side TEC to correct the bias difference [purple solid curve in Fig. 5(b)]. After leveling, we calibrate the TEC and finally retrieve the electron density profile by using the Abel inversion ($N_e(p)_{\text{retrieved}}$).

The objective function for searching the optimum pair of $N_e(p_{hmF2})$, H_0, and dH/dp consists of two terms. The first term is for assessing the agreement between the modeled occultation side TEC and the true (real observed) occultation side TEC from the POD antenna. The second term is for evaluating the consistency of the electron density slope at the modeled electron density profile with that at the true observations (i.e., smooth transition).

The degree of agreement between the true and modeled occultation side TEC values is assessed using the indicator in (15). This is defined as the summation of the average and standard deviations of absolute TEC differences between the modeled and true TEC values

$$\text{indicator} = \frac{1}{n}\sum_{i=\min}^{\max} |\Delta\text{TEC}(h_i)| + \sqrt{\frac{1}{n-1}\sum_{i=\min}^{\max}\left(|\Delta\text{TEC}(h_i)| - \frac{1}{n}\sum_{i=\min}^{\max}|\Delta\text{TEC}(h_i)|\right)^2} \tag{15}$$

where

$$\Delta\text{TEC}(h) = \text{TEC}_{\text{modeled}}(h) - \text{TEC}_{\text{true}}(h).$$

n is the number of samples and $h_{\min}$ and $h_{\max}$ are the minimum and maximum altitudes, respectively, of the occultation side TEC observed by a POD antenna. A small value of the indicator indicates a strong agreement between the modeled TEC values and the actual observed TEC values obtained from the POD antenna.

The agreement of the electron density slope is assessed by using ΔN_e slope, which is defined as

$$\Delta N_e \text{ slope} = \text{slope 1} - \text{slope 2}. \tag{16}$$

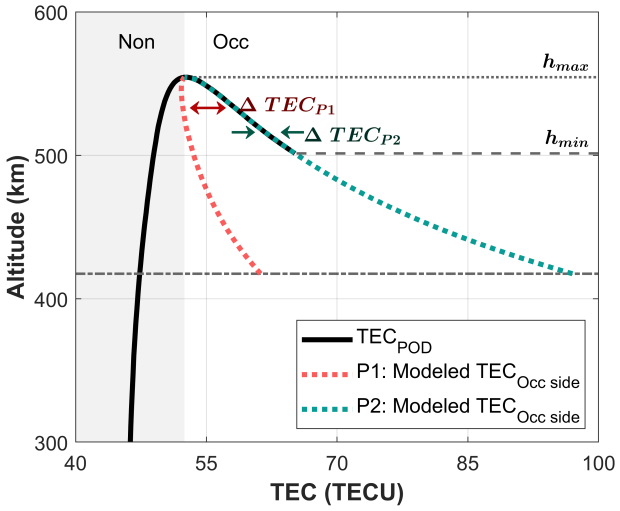

(a)

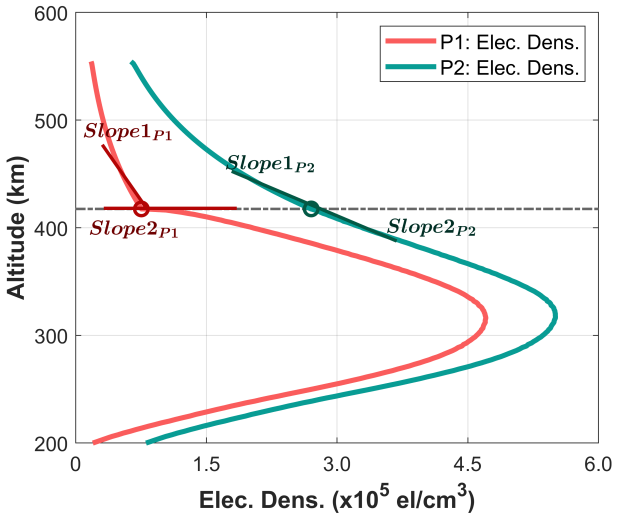

(b)

Fig. 8. Illustration of ΔTEC (a) and ΔN_e slope (b) with two example pairs ($P1$ and $P2$). (a) ΔTEC is defined as the difference between the observed TEC (black solid curve) and modeled TEC (dotted curves) on the occultation side (Occ) within the altitude where POD antenna data are available. In the diagram, pair $P2$ (green dotted curve) shows the best fit to the observations, with the smallest ΔTEC. (b) ΔN_e slope is defined as the difference in slopes of the density profiles above and below the occultation antenna TEC termination altitude (gray dash-dotted line). The smallest ΔN_e slope is seen in the results from pair $P2$, indicating smooth connection of two profiles.

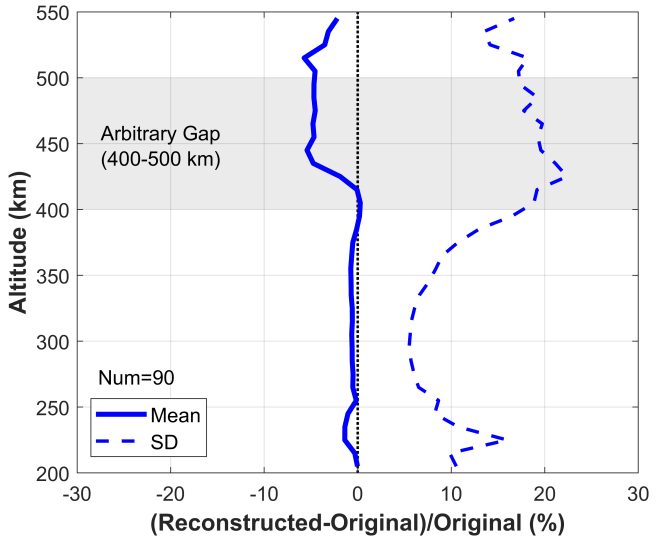

Fig. 9. Mean (blue solid curve) and standard deviation (blue dashed curve) of the percentage differences between the electron density profiles of Type A events and those reconstructed from arbitrarily masked data. These results are derived using 90 Type A events from KOMPSAT-5 observations. The range of the arbitrary gap is indicated by the gray shadow region.

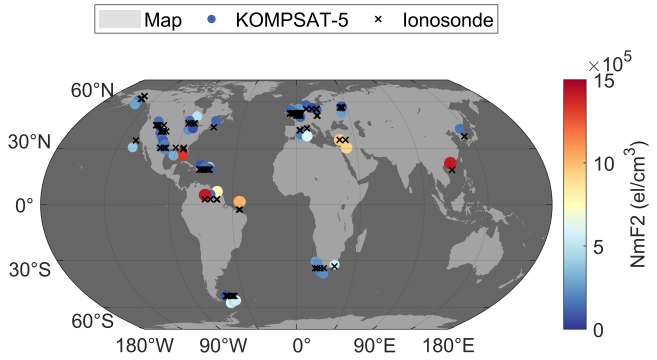

Fig. 10. Geographic distribution of collocated peak density observations from KOMPSAT-5 (represented by filled circles) and ionosonde stations (denoted by black crosses). The color scheme of the circle markers corresponds to the NmF2 values as indicated in the accompanying color bar.

Slope 1 is the slope of the modeled electron density profile, determined using a few points around the connecting point. Slope 2 is the slope of the electron density profile from the observed data.

Fig. 8 illustrates the definitions of ΔTEC and ΔN_e slope with two example pairs ($P1$ and $P2$). With respect to the altitude where the occultation antenna data terminate, the lower part is where the data from the occultation antenna exists, and the upper part is where there are no data. According to Fig. 8(a), the modeled occultation side TEC using pair $P2$ (green dotted curve) shows the closest match with the true occultation side TEC (black solid curve) obtained from the POD antenna. In Fig. 8(b), ΔN_e slope is the slope difference between slope 1 and slope 2. Its value is the smallest for pair $P2$ (green curve), ensuring a smooth transition of the data at the connecting point of two different outcomes.

The objective function for determining the optimal values of $N_e(p_{hmF2})$, H_0, and dH/dp is defined as the minimization of (17), which is the sum of the squares of (15) and (16)

$$\text{Objective function} = \text{indicator}^2 + \Delta N_e \text{ slope}^2. \quad (17)$$

As the indicator and ΔN_e slope have similar scales, additional weighting is not applied to the objective function.

The optimum pair is searched within the initial set range using the interior-point method. If the optimum value of $F2$ peak density ($N_e(p_{hmF2})_{\text{opt.}}$) searched from the initial set range differs significantly from the $F2$ peak density in the retrieved electron density profile ($N_e(p_{hmF2})_{\text{retrieved}}$), the maximum value of the $F2$ peak density range is updated to $N_e(p_{hmF2})_{\text{retrieved}}$ and the searching process is re-conducted until the absolute difference between $N_e(p_{hmF2})_{\text{opt.}}$ and $N_e(p_{hmF2})_{\text{retrieved}}$ becomes smaller than the threshold (e.g., less than 10% of the $F2$ peak density from the retrieved electron density profile).

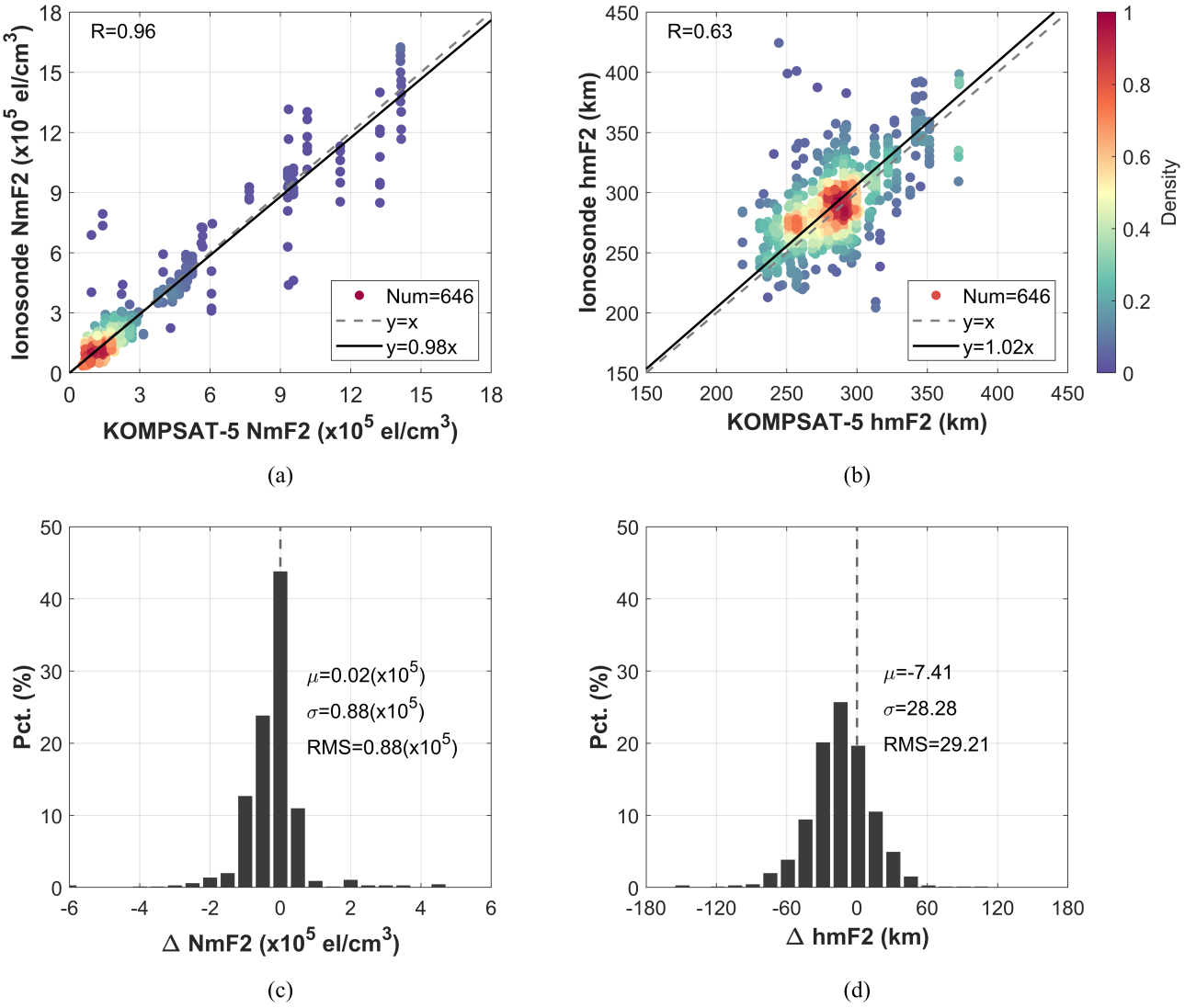

Fig. 11. Comparison of ionospheric parameters (NmF2 and hmF2) retrieved from KOMPSAT-5 observations and those from ionosonde observations. (a) and (b) Scatter plots of the KOMPSAT-5 NmF2 and hmF2 against collocated ionosonde measurements. The black solid lines represent the best-fit line, while gray dashed lines denote $y = x$. The color scale indicates the density of the data points. (c) and (d) Percentage distributions of NmF2 and hmF2 differences between KOMPSAT-5 and ionosonde observations.

By applying the final optimum pair of the three parameters to (11), (13), and (14), we connect the TEC data from the POD and occultation antennas by filling the gap between the two antennas' data with the modeled occultation side TEC. Subsequently, we obtain the calibrated TEC from the connected data and retrieve the final electron density profile.

V. Validation of the Proposed Method Using KOMPSAT-5 Data

A. Validation of the Modeled Remaining Gap

We first validate the method described in Section IV-C using Type A events selected from KOMPSAT-5 observations. The validation process involves artificially removing (or masking) a portion of the data. This masking transforms Type A events into Type B events. Arbitrary data gaps are introduced in the 400–500 km altitude range in the occultation side observations for 90 Type A events from KOMPSAT-5 during the year 2015. The method described in Section IV-C is then applied to retrieve the electron density profiles from the arbitrarily masked data. Fig. 9 presents the statistics of the percentage differences between the electron density profiles retrieved from the original Type A events and those retrieved from the arbitrarily masked data. The percentage differences within the altitude range of 200–550 km are binned by 10 km altitude bins and the statistics are calculated for each bin. In Fig. 9, the mean values are illustrated by the blue solid curve and the standard deviation values are represented by the blue dashed curve. The mean ranges from −5.7% to 0.3%, and the standard deviation ranges from 5.5% to 22.4%. Within the arbitrary gap region, the mean and standard deviation values are relatively larger than those in other altitude regions. This could be attributed to either the relatively small value of electron density in higher altitudes or modeling error. At altitudes below 400 km, the mean values are nearly zero across all altitudes. The increase in standard deviation below 250 km may also be attributed to smaller values of the electron density in this altitude region. Both the mean and standard

deviation values for altitude around the $F2$ peak height region (altitude between 250 and 350 km according to the analyzed 90 profiles) remain within approximately 10%.

B. Comparison Between Ionospheric Parameters Retrieved From KOMPSAT-5 and Ionosonde Measurements

The ionospheric parameters retrieved from KOMPSAT-5 data by applying our proposed method are compared with those derived from collocated digital ionosonde observations. Our investigation focuses on two ionospheric parameters: $F2$ peak density (NmF2) and $F2$ peak height (hmF2). In this analysis, the time window between the two datasets is limited to 30 min and a maximum 5° (∼500 km) longitude/latitude difference is set as the criterion for collocation. This collocation criterion is comparable to or within the collocation window defined in other previous studies (2° from [27], 5° from [9], 1200 km from [3], and 1800 km from [5]). The dataset used for the validation covers the year 2015, coinciding with the initiation of RO data provision from the KOMPSAT-5 mission and near the solar maximum during solar cycle 24 (April 2014).

Fig. 10 shows the geographic distribution of collocated peak density observations from KOMPSAT-5 (represented by filled circles) and ionosonde stations (denoted by black crosses). The color scheme of the circle markers corresponds to the NmF2 values, as indicated in the accompanying color bar. There are 31 collocated ionosonde stations, and the total number of collocated events is 646.

Fig. 11 provides a comprehensive visualization through scatter plots of NmF2 and hmF2, along with histograms illustrating the distribution of differences compared to ionosonde observations. With a total of 646 data points analyzed, NmF2 values derived from KOMPSAT-5 are in good agreement with those from ionosondes, as indicated by the high correlation coefficient value of 0.96 [Fig. 11(a)]. The distribution of NmF2 deviations is shown in Fig. 11(c). The mean NmF2 difference is 0.02×10^5 el/cm^3, with both the standard deviation and root-mean-square (rms) being 0.88×10^5 el/cm^3. These values are comparable to those reported in previous studies for other missions (e.g., CHAMP: mean value of 0.7×10^5 el/cm^3 and rms value of $1.0-2.5 \times 10^5$ el/cm^3 [46], COSMIC-1: mean value of $-0.2-1.2 \times 10^5$ el/cm^3 and standard deviation value of $0.6-1.9 \times 10^5$ el/cm^3 [47], MetOp-A: mean value of 0.05×10^5 el/cm^3 and standard deviation value of 1.10×10^5 el/cm^3 [11], and Spire Global: mean value of -0.15×10^5 el/cm^3 and rms value of 1.07×10^5 el/cm^3 [48]). According to Fig. 11(b), the hmF2 values retrieved from KOMPSAT-5 exhibit a clear linear relationship with those derived from ionosonde observations, as indicated by the slope (1.02) of the best fit line being close to 1.0. However, the correlation coefficient is relatively lower (0.63) compared to that of NmF2. It is important to note that there may be limitations in the accuracy of hmF2 derived from ionosonde measurements, as its accuracy strongly depends on the performance of the true height inversion algorithm. The distribution of hmF2 deviations is depicted in Fig. 11(d). The mean value of hmF2 differences is −7.41 km, with standard deviation and rms values of 28.28 and 29.21 km, respectively. The statistics of hmF2 differences are also comparable to those from other missions (e.g., COSMIC-1: mean value of −7.0−7.5 km and standard deviation value of 24−48 km [47], COSMIC-2: mean of 4.16 km and standard deviation of 19.57 km [9], MetOp-A: mean of −2.4 km and standard deviation of −36 km [11], and Spire Global: mean of −7.71 km and rms of 27.13 km [48]).

VI. Conclusion

This study aims to retrieve electron density profiles from RO data using the calibration technique, even in cases where non-occultation side observations are missing (common in many RO missions). To address this challenge, we proposed a multiantenna-based data gap filling method that connects the observations from the POD and occultation antennas and models the remaining data gap between them. We evaluated the proposed method by modeling the ionosphere in the remaining data gaps, which were arbitrarily masked from KOMPSAT-5 RO data. The results show that our proposed method can effectively reconstruct the ionosphere in the arbitrary gap regions, with nearly identical profiles to the original data. We applied the proposed method to the KOMPSAT-5 data processing and compared the resulting electron densities with those obtained independently from ionosonde observations. The ionospheric parameters derived from our method exhibit good agreement with those from ionosonde observations. The validation results demonstrate that our method effectively fills and corrects the ionospheric information above the LEO altitude by connecting the observations from the POD and occultation antennas.

This proposed method presents the possibility of using POD antenna observations to correct ionospheric information above the LEO altitude. This approach can be applied to other RO missions with similar antenna placements and data observability. This proposed method relies on the coverage of POD antenna observations on the non-occultation side. If there is a large gap between the data from two antennas, or if there is no POD antenna data on the non-occultation side, additional modeling or alternative methods, such as those described in [10], [23], and [24], may need to be employed. Therefore, we plan to extend our algorithm to include modeling for significantly large gaps between the POD and occultation antenna data.

Acknowledgment

The RO data (COSMIC, CHAMP, KOMPSAT-5) are provided by COSMIC Data Analysis and Archive Center, and ionosonde observations are provided by Global Ionospheric Radio Observatory.

References

[1] T. P. Yunck, G. F. Lindal, and C.-H. Liu, "The role of GPS in precise Earth observation," in *Proc. IEEE PLANS Position Location Navigat. Symp., Rec. Navigat. Into 21st Century.*, Orlando, FL, USA, Nov. 1988, pp. 251–258, doi: 10.1109/PLANS.1988.195491.

[2] G. A. Hajj and L. J. Romans, "Ionospheric electron density profiles obtained with the global positioning system: Results from the GPS/MET experiment," *Radio Sci.*, vol. 33, no. 1, pp. 175–190, Jan. 1998, doi: 10.1029/97RS03183.

[3] W. S. Schreiner, S. V. Sokolovskiy, C. Rocken, and D. C. Hunt, "Analysis and validation of GPS/MET radio occultation data in the ionosphere," *Radio Sci.*, vol. 34, no. 4, pp. 949–966, Jul. 1999, doi: 10.1029/1999RS900034.

[4] S. Sokolovskiy, W. Schreiner, C. Rocken, and D. Hunt, "Detection of high-altitude ionospheric irregularities with GPS/MET," *Geophys. Res. Lett.*, vol. 29, no. 3, pp. 3-1–3-4, Feb. 2002, doi: 10.1029/2001gl013398.

[5] N. Jakowski et al., "GPS radio occultation measurements of the ionosphere from CHAMP: Early results," *Geophys. Res. Lett.*, vol. 29, no. 10, pp. 95-1–95-4, May 2002, doi: 10.1029/2001gl014364.

[6] R. A. Anthes et al., "The COSMIC/FORMOSAT-3 mission: Early results," *Bull. Amer. Meteorolog. Soc.*, vol. 89, no. 3, pp. 313–334, Mar. 2008, doi: 10.1175/bams-89-3-313.

[7] X. Yue, W. S. Schreiner, Y-H. Kuo, D. C. Hunt, and C. Rocken, "GNSS radio occultation technique and space weather monitoring," in *Proc. I_{ON} GNSS+*, Nashville, TN, USA, 2013, pp. 2508–2522.

[8] C. Lin et al., "The early results and validation of FORMOSAT-7/COSMIC-2 space weather products: Global ionospheric specification and ne-aided Abel electron density profile," *J. Geophys. Res., Space Phys.*, vol. 125, no. 10, Oct. 2020, Art. no. e2020JA028028, doi: 10.1029/2020ja028028.

[9] I. Cherniak et al., "Accuracy assessment of the quiet-time ionospheric F2 peak parameters as derived from COSMIC-2 multi-GNSS radio occultation measurements," *J. Space Weather Space Climate*, vol. 11, p. 18, Feb. 2021, doi: 10.1051/swsc/2020080.

[10] M. M. Hoque et al., "A new method of electron density retrieval from MetOp–A's truncated radio occultation measurements," *Remote Sens.*, vol. 15, no. 5, p. 1424, Mar. 2023, doi: 10.3390/rs15051424.

[11] M. M. Hoque et al., "Assessment of GRAS ionospheric measurements for ionospheric model assimilation," *Remote Sens.*, vol. 15, no. 12, p. 3129, Jun. 2023, doi: 10.3390/rs15123129.

[12] T. Mao et al., "First ionospheric radio-occultation measurements from GNSS occultation sounder on the Chinese Feng-Yun 3C satellite," *IEEE Trans. Geosci. Remote Sens.*, vol. 54, no. 9, pp. 5044–5053, Sep. 2016, doi: 10.1109/TGRS.2016.2546978.

[13] W.-K. Lee et al., "Retrieval of electron density profile for KOMPSAT-5 GPS radio occultation data processing system," *J. Astron. Space Sci.*, vol. 24, no. 4, pp. 297–308, Dec. 2007, doi: 10.5140/JASS.2007.24.4.297.

[14] A. G. Burns, S. C. Solomon, W. Wang, L. Qian, Y. Zhang, and L. J. Paxton, "Daytime climatology of ionospheric NmF2 and hmF2 from COSMIC data," *J. Geophys. Res., Space Phys.*, vol. 117, no. A9, Sep. 2012, Art. no. A09315, doi: 10.1029/2012ja017529.

[15] C. H. Lin et al., "Motions of the equatorial ionization anomaly crests imaged by FORMOSAT-3/COSMIC," *Geophys. Res. Lett.*, vol. 34, no. 19, Oct. 2007, Art. no. L19101, doi: 10.1029/2007gl030741.

[16] X. Luan, P. Wang, X. Dou, and Y. C. Liu, "Interhemispheric asymmetry of the equatorial ionization anomaly in solstices observed by COSMIC during 2007–2012," *J. Geophys. Res., Space Phys.*, vol. 120, no. 4, pp. 3059–3073, Apr. 2015, doi: 10.1002/2014ja020820.

[17] I. T. Lee et al., "Assimilation of FORMOSAT-3/COSMIC electron density profiles into a coupled thermosphere/ionosphere model using ensemble Kalman filtering," *J. Geophys. Res., Space Phys.*, vol. 117, no. A10, Oct. 2012, Art. no. A10318, doi: 10.1029/2012ja017700.

[18] T. Matsuo and C.-T. Hsu, "Inference of hidden states by coupled thermosphere-ionosphere data assimilation," in *Upper Atmosphere Dynamics and Energetics*. Hoboken, NJ, USA: Wiley, 2021, pp. 343–363, doi: 10.1002/9781119815631.ch18.

[19] C. Hwang, T.-P. Tseng, T.-J. Lin, D. Švehla, U. Hugentobler, and B. F. Chao, "Quality assessment of FORMOSAT-3/COSMIC and GRACE GPS observables: Analysis of multipath, ionospheric delay and phase residual in orbit determination," *GPS Solutions*, vol. 14, no. 1, pp. 121–131, Jan. 2010, doi: 10.1007/s10291-009-0145-0.

[20] T.-P. Tseng et al., "Assessing antenna field of view and receiver clocks of COSMIC and GRACE satellites: Lessons for COSMIC-2," *GPS Solutions*, vol. 18, no. 2, pp. 219–230, Apr. 2014, doi: 10.1007/s10291-013-0323-y.

[21] J.-P. Weiss, D. Hunt, W. Schreiner, T. VanHove, D. Arnold, and A. Jaeggi, "COSMIC-2 precise orbit determination results," presented at the 22nd EGU General Assembly, May 2020. [Online]. Available: https://presentations.copernicus.org/EGU2020/EGU2020-20170_presentation.pdf

[22] N. Jakowski, "Ionospheric GPS radio occultation measurements on board CHAMP," *GPS Solutions*, vol. 9, no. 2, pp. 88–95, Jun. 2005, doi: 10.1007/s10291-005-0137-7.

[23] M. Hernández-Pajares et al., "Electron density extrapolation above F2 peak by the linear vary-chap model supporting new global navigation satellite systems-LEO occultation missions," *J. Geophys. Res., Space Phys.*, vol. 122, no. 8, pp. 9003–9014, Aug. 2017, doi: 10.1002/2017ja023876.

[24] H. Lyu, M. Hernández-Pajares, E. Monte-Moreno, and E. Cardellach, "Electron density retrieval from truncated radio occultation GNSS data," *J. Geophys. Res., Space Phys.*, vol. 124, no. 6, pp. 4842–4851, Jun. 2019, doi: 10.1029/2019ja026744.

[25] M. Hernández-Pajares, J. M. Juan, and J. Sanz, "New approaches in global ionospheric determination using ground GPS data," *J. Atmos. Solar-Terr. Phys.*, vol. 61, no. 16, pp. 1237–1247, Nov. 1999, doi: 10.1016/s1364-6826(99)00054-1.

[26] J. Lei et al., "Comparison of COSMIC ionospheric measurements with ground-based observations and model predictions: Preliminary results," *J. Geophys. Res., Space Phys.*, vol. 112, no. A7, Jul. 2007, Art. no. A07308, doi: 10.1029/2006ja012240.

[27] X. Wu, X. Hu, X. Gong, X. Zhang, and X. Wang, "Analysis of inversion errors of ionospheric radio occultation," *GPS Solutions*, vol. 13, no. 3, pp. 231–239, Jan. 2009, doi: 10.1007/s10291-008-0116-x.

[28] E. Sardón, A. Rius, and N. Zarraoa, "Estimation of the transmitter and receiver differential biases and the ionospheric total electron content from global positioning system observations," *Radio Sci.*, vol. 29, no. 3, pp. 577–586, May 1994, doi: 10.1029/94RS00449.

[29] A. Manucci, B. Iijima, U. Lindqwister, X. L. Sparks, and B. Wilson, "GPS and ionosphere," Revised Submission URSI Rev. Radio Sci., Jet Propuls. Lab., Pasadena, CA, USA, 1999. [Online]. Available: https://hdl.handle.net/2014/16838

[30] M. Hernández-Pajares et al., "The ionosphere: Effects, GPS modeling and the benefits for space geodetic techniques," *J. Geodesy*, vol. 85, no. 12, pp. 887–907, Sep. 2011, doi: 10.1007/s00190-011-0508-5.

[31] V. V. Forsythe, T. Duly, D. Hampton, and V. Nguyen, "Validation of ionospheric electron density measurements derived from spire CubeSat constellation," *Radio Sci.*, vol. 55, no. 1, pp. 1–13, Jan. 2020, doi: 10.1029/2019RS006953.

[32] *COSMIC Data Analysis and Archive Center (CDAAC). Algorithms for Inverting Radio Occultation Signals in the Ionosphere*. Accessed: Dec. 1, 2023. [Online]. Available: https://cdaac-www.cosmic.ucar.edu/cdaac/doc/documents/gmrion.pdf

[33] S. Syndergaard, E. R. Kursinski, B. M. Herman, E. M. Lane, and D. E. Flittner, "A refractive index mapping operator for assimilation of occultation data," *Monthly Weather Rev.*, vol. 133, no. 9, pp. 2650–2668, Sep. 2005, doi: 10.1175/mwr3001.1.

[34] S. Syndergaard, W. S. Schreiner, C. Rocken, D. C. Hunt, and K. F. Dymond, "Preparing for COSMIC: Inversion and analysis of ionospheric data products," in *Atmosphere and Climate*. New York, NY, USA: Springer, 2006, pp. 137–146, doi: 10.1007/3-540-34121-8_12.

[35] R. Leitinger, H.-P. Ladreiter, and G. Kirchengast, "Ionosphere tomography with data from satellite reception of global navigation satellite system signals and ground reception of navy navigation satellite system signals," *Radio Sci.*, vol. 32, no. 4, pp. 1657–1669, Jul. 1997, doi: 10.1029/97RS01027.

[36] K.-M. Roh and Y. Hwang, "Performance comparison of KOMPSAT-5 precision orbit determination with GRACE," *Int. J. Aerosp. Eng.*, vol. 2020, pp. 1–11, Feb. 2020, doi: 10.1155/2020/7358286.

[37] S. Chapman, "The absorption and dissociative or ionizing effect of monochromatic radiation in an atmosphere on a rotating Earth," *Proc. Phys. Soc.*, vol. 43, no. 1, pp. 26–45, Jan. 1931, doi: 10.1088/0959-5309/43/1/305.

[38] P. S. Epstein, "Refection of waves in an inhomogeneous absorbing medium," *Proc. Nat. Acad. Sci. USA*, vol. 16, no. 10, pp. 627–637, Oct. 1930, doi: 10.1073/pnas.16.10.627.

[39] C. Fonda, P. Coïsson, B. Nava, and S. M. Radicella, "Comparison of analytical functions used to describe topside electron density profiles with satellite data," *Ann. Geophysics*, vol. 48, no. 3, pp. 491–495, Dec. 2009, doi: 10.4401/ag-3213.

[40] K. Rawer, "Synthesis of ionospheric electron density profiles with Epstein functions," *Adv. Space Res.*, vol. 8, no. 4, pp. 191–199, Jan. 1988, doi: 10.1016/0273-1177(88)90239-6.

[41] S. M. Stankov, N. Jakowski, S. Heise, P. Muhtarov, I. Kutiev, and R. Warnant, "A new method for reconstruction of the vertical electron density distribution in the upper ionosphere and plasmasphere," *J. Geophys. Res., Space Phys.*, vol. 108, no. A5, pp. SIA 1-1–SIA 1-21, May 2003, doi: 10.1029/2002ja009570.

[42] A. Pignalberi, M. Pezzopane, D. R. Themens, H. Haralambous, B. Nava, and P. Coïsson, "On the analytical description of the topside ionosphere by NeQuick: Modeling the scale height through COSMIC/FORMOSAT-3 selected data," *IEEE J. Sel. Topics Appl. Earth Observ. Remote Sens.*, vol. 13, pp. 1867–1878, 2020, doi: 10.1109/JSTARS.2020.2986683.

[43] A. Pignalberi, M. Pezzopane, B. Nava, and P. Coïsson, "On the link between the topside ionospheric effective scale height and the plasma ambipolar diffusion, theory and preliminary results," *Sci. Rep.*, vol. 10, no. 1, Oct. 2020, Art. no. 17541, doi: 10.1038/s41598-020-73886-4.

[44] R. H. Byrd, J. C. Gilbert, and J. Nocedal, "A trust region method based on interior point techniques for nonlinear programming," *Math. Program.*, vol. 89, no. 1, pp. 149–185, Nov. 2000, doi: 10.1007/pl00011391.

[45] R. H. Byrd, M. E. Hribar, and J. Nocedal, "An interior point algorithm for large-scale nonlinear programming," *SIAM J. Optim.*, vol. 9, no. 4, pp. 877–900, Jan. 1999, doi: 10.1137/s1052623497325107.

[46] N. Jakowski et al., "Validation of GPS ionospheric radio occultation results onboard CHAMP by vertical sounding observations in Europe," in *Earth Observation With CHAMP*. New York, NY, USA: Springer, 2005, pp. 447–452, doi: 10.1007/3-540-26800-6_70.

[47] M. Limberger, M. Hernández-Pajares, A. Aragón-Ángel, D. Altadill, and D. Dettmering, "Long-term comparison of the ionospheric F2 layer electron density peak derived from ionosonde data and formosat-3/COSMIC occultations," *J. Space Weather Space Climate*, vol. 5, p. A21, Jul. 2015, doi: 10.1051/swsc/2015023.

[48] L. Liu and Y. J. Morton, "Assessment of storm-time ionospheric electron density measurements from spire global CubeSat GNSS radio occultation constellation," *GPS Solutions*, vol. 27, no. 2, pp. 1-11–11-11, Feb. 2023, doi: 10.1007/s10291-023-01414-8.

Hyeyeon Chang received the B.S. and Ph.D. degrees from the Aerospace Engineering Department, KAIST, Daejeon, South Korea, in 2016 and 2023, respectively.

The Ph.D. work was focused on GNSS radio occultation (RO) ionospheric electron density retrieval. She is currently a Post-Doctoral Researcher with the Satellite Navigation and Sensing Laboratory, University of Colorado, Boulder, CO, USA. Her research interests include GNSS remote sensing techniques and ionospheric dynamics.

Woo Kyoung Lee received the B.S. and M.S. degrees in astronomy and space science from Yonsei University, Seoul, South Korea, in 2002 and 2004, respectively, and the Ph.D. degree in astronomy and space science from the University of Science and Technology, Daejeon, South Korea, in 2011.

She is a Principal Researcher with the Korea Astronomy and Space Science Institute, Daejeon. She is currently leading efforts to develop a near-real-time ionospheric monitoring system using GNSS and a space-borne camera for observing auroras and airglow from low Earth orbit.

Hyosub Kil received the B.S. and M.S. degrees in astronomy from Seoul National University, Seoul, South Korea, in 1991 and 1993, respectively, and the Ph.D. degree in physics from the University of Texas at Dallas, Richardson, TX, USA, in 1997.

He is currently a Principal Professional Staff Member with the Johns Hopkins University Applied Physics Laboratory, Laurel, MD, USA. His research interests include the Earth's ionosphere, focusing on ionospheric dynamics, equatorial plasma bubbles, traveling ionospheric disturbances, and plasma–neutral coupling.

Hyosang Yoon received the B.S. and M.S. degrees in aerospace engineering from KAIST, Daejeon, South Korea, in 2008 and 2010, respectively, and the Ph.D. degree in aeronautics and astronautics from MIT, Cambridge, MA, USA, in 2017.

He is an Assistant Professor with the Department of Aerospace Engineering, KAIST. His research interests include satellite systems and GNSS radio occultation (RO) using small satellites.

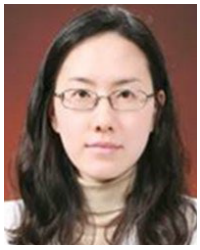

Jiyun Lee (Member, IEEE) received the B.S. degree in astronomy and atmospheric science from Yonsei University, Seoul, South Korea, in 1997, the M.S. degree in aerospace engineering sciences from the University of Colorado, Boulder, CO, USA, in 1999, and the Ph.D. degree in aeronautics and astronautics from Stanford University, Stanford, CA, USA, in 2005.

She is a KAIST Endowed Chair Professor with the Department of Aerospace Engineering, Korea Advanced Institute of Science and Technology, Daejeon, South Korea. As part of her professional experience, she worked as a Consulting Professor with Stanford University, a Principal Systems Engineer with Tetra Tech AMT, Los Angeles, CA, USA, and a Senior GPS Systems Engineer with SiRF Technology, Inc., San Jose, CA, USA. She has published more than 300 research papers in the field of GNSS applications, multisensor navigation, safety-critical systems, atmospheric science, and remote sensing.

Dr. Lee was awarded the FAA Recognition Award in 2008 and 2013, and the Colonel Thomas L. Thurlow Award of the Institute of Navigation in 2023.